

## Scattering of Internal Waves at Finite Topography in Two Dimensions. Part I: Theory and Case Studies

PETER MÜLLER AND XIANBING LIU

*Department of Oceanography, University of Hawaii at Manoa, Honolulu, Hawaii*

(Manuscript received 3 December 1998, in final form 1 April 1999)

### ABSTRACT

The scattering of internal gravity waves at finite topography in two dimensions is studied theoretically and numerically for a finite depth ocean. A formal solution is derived using a mapping function based on ray tracing. The solution satisfies radiation conditions. Energy is conserved. The incoming energy flux is redistributed in physical and modenumber space. Numerical solutions are calculated for a single plane wave propagating from the ocean side onto slope–shelf configurations where a flat shallow shelf is connected to a flat deep ocean by linear slopes, staircases, convex or concave parabolic profiles, and half-cosine slopes. The fraction of the incoming energy flux transmitted onto the shelf and reflected back to the deep ocean and the distribution of these fluxes in modenumber space are calculated. The results depend on the parameters of the incident wave and of the topography. Especially important is the distinction between supercritical topography, where the slope of the topography exceeds the wave slope, and subcritical topography. Results obtained are (i) for subcritical topography nearly all of the incoming energy flux is transmitted onto the shelf; (ii) for supercritical topography part is transmitted onto the shelf and part is reflected back to the deep ocean; the partition depends on the incident modenumber and the shelf to ocean depth ratio; (iii) for a linear slope the distribution of the transmitted and reflected fluxes in modenumber space shows peaks at modenumbers roughly consistent with reflection laws; (iv) more of the incident wave energy flux is scattered to higher than to lower modenumbers, especially for near-critical topography; (v) convex slopes are more efficient in scattering the energy flux to high modenumbers than concave slopes; (vi) major differences occur when a linear slope is represented by a series of steps, especially for subcritical topography and high incident modenumbers; and (vii) the scattering results differ in important aspects from the results obtained by reflection theory, especially for supercritical topography and low incident modenumbers. Scattering at ridge configurations is also considered. The results can be inferred from the results for the slope–shelf configurations. The extension to a superposition of incident waves with a realistic spectrum and the implications for internal wave-induced boundary mixing are treated in Part II.

### 1. Introduction

The scattering of linear internal gravity waves at bottom topography redistributes the incoming energy flux both in physical and wavenumber space. The details of this redistribution depend on the frequency and wavenumber of the incident wave and on the properties of the topography. The reflection off an infinite straight slope was studied in two dimensions by Phillips (1966) and later in three dimensions by Eriksen (1982). The somewhat peculiar reflection laws arise from the fact that the internal-wave wavenumber vector maintains its angle with the vertical axis rather than with the normal vector of the topography, as in specular reflection. Specifically, the reflection laws imply “critical” reflection when the slope of the wave approaches the slope of the

topography. The reflected wave then has an infinite wavenumber and zero group velocity. Energy and shear increase beyond bound at the sloping topography.

The reflection off a straight slope is an appropriate limit only for short waves whose wavelengths are smaller than the radius of curvature of the topography. For longer waves, one must take the full structure of the topography into account and must consider the scattering off a curved surface. The scattering in two dimensions was first studied by Baines (1971a,b) for the case that an internal wave propagates from above onto an ocean bottom. The ocean has no upper surface. Baines showed that the scattering problem can be reduced to solving a coupled pair of Fredholm integral equations of the second kind. In particular, he showed that the implementation of radiation conditions leads to the backscattering of internal wave energy off curved bottom topography, a process that is absent in the reflection theory applied earlier to the scattering problem (e.g., Longuet-Higgins 1966). Reflection theory determines the scattered wave field by applying the reflection laws to the tangent plane of the topography.

---

*Corresponding author address:* Dr. Peter Müller, Department of Oceanography, University of Hawaii at Manoa, 1000 Pope Rd, MSB 429, Honolulu, HI 96822.  
E-mail: pmuller@iniki.soest.hawaii.edu

In this paper, we study the two-dimensional scattering problem for a finite depth ocean. The wave propagates in from the side. This geometry must be adopted for the generation of internal tides by the barotropic surface tide (see Baines 1974, 1982; Sandstrom 1976) and is the more appropriate geometry for oceanic applications since most of the oceanic internal wave energy resides in low modenumber waves that have vertical scales only slightly less than the ocean depth. Furthermore, we study the scattering at finite topography. The topography can have an arbitrary height and shape, except that it must be localized. The bottom must be flat in the far field. The topographic configurations that we have in mind are slope–shelf and ridge configurations. The scattering at infinitesimal topography has been studied by perturbation methods (e.g., Cox and Sandstrom 1962; Rubenstein 1988; Müller and Xu 1992). The expansions require that (i) the height of the topography be smaller than the vertical wavelength of the wave and (ii) that the slope of the topography be smaller than the wave slope. Because the wave slope approaches zero as the wave frequency approaches the Coriolis frequency, the perturbation expansions break down for near-inertial internal gravity waves, which, again, contain most of the oceanic internal wave energy. While consideration of a finite depth ocean and of finite topography are steps towards realism, the restriction to two dimensions is, of course, a major idealization.

In Part I of this paper, we consider the scattering of a single incoming plane wave of specified frequency and modenumber. Results for a more complicated incoming wave field can be obtained by superposition since the scattering problem is linear in the incident internal wave amplitude. The oceanographically relevant case of an incoming internal wave field with a Garrett and Munk spectrum is studied in Müller and Liu (2000, hereafter Part II), with particular emphasis on how much mixing can be induced by the scattering process.

Part I is organized as follows. First, we derive a formal solution to the scattering problem. It uses characteristic coordinates and a mapping function based on ray tracing (Sandstrom 1976). An important property of the solution is that the depth-integrated energy flux is constant. The incoming energy flux is partly transmitted or forwardscattered and partly reflected or backward-scattered and redistributed in modenumber space. Section 3 discusses the two analytical solutions that are known to us: the scattering at a knife edge barrier (Larsen 1969) and the scattering at topography with a linear mapping function. Section 4 introduces our numerical solution technique. We test its accuracy against the knife edge analytical solution and show that it converges with increasing resolution. In section 5, we numerically calculate the scattering of a single plane wave propagating from the ocean side onto a slope–shelf configuration where a flat shallow shelf is connected to a flat deep ocean by a variety of slope profiles. Results for ridge

configurations can easily be inferred from the results for the slope–shelf configurations. The redistribution of the incoming energy flux depends on the frequency and modenumber of the incoming wave and on the properties of the topography. We compare our results to the results from reflection theory and investigate issues such as replacing a slope by a series of steps and the difference between convex and concave curvature. Section 6 summarizes and discusses our major findings from these studies.

## 2. Theory

### a. Wave equation

In two dimensions the internal wave equation is given by (see appendix A)

$$[N^2(z) + \partial_{tt}] \partial_{xx} \psi + (\partial_{tt} + f^2) \partial_{zz} \psi = 0, \quad (1)$$

where  $x$  is the horizontal coordinate,  $z$  the vertical coordinate,  $t$  the time coordinate,  $N(z)$  the Brunt–Väisälä frequency,  $f$  the Coriolis frequency, and  $\psi(x, z, t)$  the streamfunction such that  $u = \partial_z \psi$  is the horizontal velocity and  $w = -\partial_x \psi$  the vertical velocity component. This wave equation has to be solved for a prescribed incoming internal wave field at  $x = +\infty$  subject to the boundary conditions that  $\psi = 0$  at the surface  $z = 0$  (rigid lid condition) and at the bottom  $z = -h(x)$  and subject to the radiation condition that the scattered field is an outgoing field at  $x = \pm\infty$ . Scattering of linear internal waves at bottom topography does not change the frequency. For an incoming monochromatic wave of frequency  $\omega$  the streamfunction can thus be written

$$\psi(x, z, t) = \Psi(x, z) \exp(-i\omega t) \quad (2)$$

and the wave equation and boundary conditions become

$$\partial_{xx} \Psi - c^2(z) \partial_{zz} \Psi = 0 \quad \text{and} \quad (3)$$

$$\Psi = 0, \quad \text{at } z = 0, z = -h(x), \quad (4)$$

where

$$c(z) = \sqrt{\frac{\omega^2 - f^2}{N^2(z) - \omega^2}} \quad (5)$$

is the wave slope. The wave slope is both the slope of the group velocity vector and the slope of the wave crests since the group velocity vector is perpendicular to the wavenumber vector for internal gravity waves. We will assume  $N = N_0 = \text{const}$  and hence  $c = c_0 = \text{const}$  in the following. In terms of the characteristic coordinates

$$\xi = x + \int_0^z \frac{dz}{c_0} \quad (6a)$$

$$\eta = x - \int_0^z \frac{dz}{c_0} \quad (6b)$$

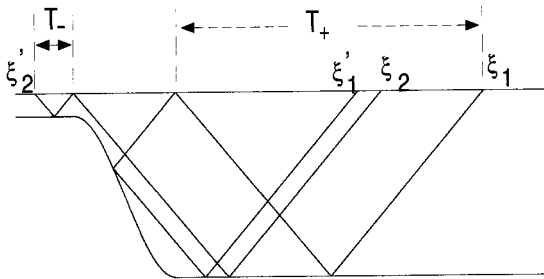


FIG. 1. Sketch of slope-shelf configuration with characteristics and  $T$ -periods.

the wave equation (3) then has the general solution

$$\Psi = \sqrt{c_0}[f(\xi) + g(\eta)] \tag{7}$$

with arbitrary functions  $f(\xi)$  and  $g(\eta)$ . Baines (1973) showed that (7), with  $c_0$  replaced by  $c(z)$ , is also the solution for stratifications that lead to profiles  $c(z) = c_0(1 + c_1z)^2$  with  $c_0$  and  $c_1$  being constants. We will not consider this possible generalization regarding the assumptions of linear waves and two-dimensionality as the more severe restriction. Lines of constant  $\xi$  and  $\eta$  are called characteristics or rays. They have slope  $\pm|c|$ . The solution (7) shows that “influence” propagates along these rays. The functions  $f$  and  $g$  have to be determined by the boundary and radiation conditions. The surface boundary condition  $\Psi = 0$  at  $z = 0$  implies

$$f(\xi) = -g(\xi) \tag{8}$$

so that one only needs to determine the function  $f$ . In his study of internal tide generation Baines (1974) showed that the implementation of the bottom boundary and radiation conditions reduces the problem to solving a pair of coupled Fredholm integral equations of the second kind for  $f(\xi)$ . However, the numerical algorithms that he used to solve these integral equations, which have a singular kernel, turned out to be unstable. We therefore resort to an alternative approach, an approach that was inspired by the work of Sandstrom (1976) and uses the mapping function to be introduced next.

*b. Mapping function*

Consider the slope-shelf configuration in Fig. 1 with open ends on both sides. The bottom boundary condition  $\Psi = 0$  at  $z = -h(x)$  implies

$$f(\xi) = f(\xi + T(\xi)), \tag{9}$$

where  $T(\xi)$  is the surface distance between two characteristics emanating from a bottom boundary point. The function  $f$  is thus periodic. The period depends on  $\xi$ . The function  $T(\xi)$  is called  $T$ -period by Sandstrom (1976). It reflects the structure of the bottom topography. For a flat bottom  $T$  is a constant. Consider two  $T$ -periods  $T_+$  and  $T_-$ , one on each side of the topography in the far field. If one traces a characteristic from one  $T$ -period, say  $T_+$ , one will end up again in one of the

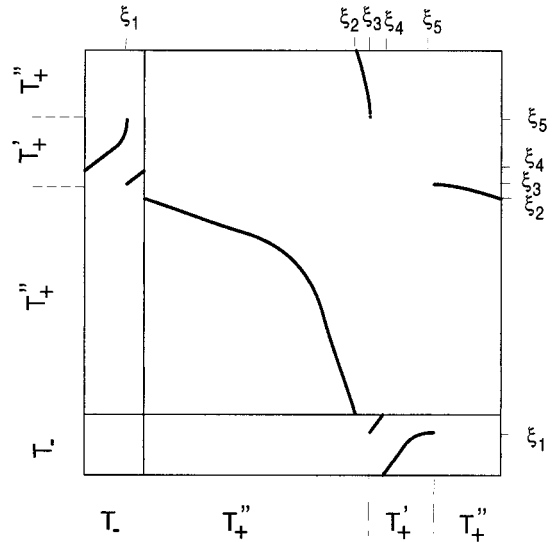


FIG. 2. Mapping function for the half-cosine slope shown in Fig. 1.  $T_+$  is the  $T$ -period on the ocean side,  $T_-$  is the  $T$ -period on the shelf side;  $T_+'$  maps onto  $T_-$ ,  $T_+''$  onto itself, and  $T_-$  onto  $T_+'$ . The mapping function is discontinuous at the points  $\xi_1, \dots, \xi_5$ .

far fields, in either  $T_+$  or  $T_-$ . In which  $T$ -period depends on whether the characteristics intersect the topography at points where the slope of the bottom is sub- or supercritical. The slope of the topography is called subcritical, critical, or supercritical if it is smaller, equal, or larger than the slope  $|c|$  of the characteristics. If the characteristic encounters a subcritical slope, it is traced forwardly, as the characteristic  $\xi_2$  in Fig. 1. If it encounters a supercritical topographic slope, it is traced backwardly, as the characteristic  $\xi_1$  in Fig. 1.

In general, the tracing establishes a mapping

$$\xi' = \mathcal{M}(\xi) \tag{10}$$

of the two  $T$ -periods onto themselves with  $\mathcal{M}(\mathcal{M}(\xi)) = \xi$ . If the slope of the topography is subcritical everywhere, then a full  $T$ -period on one side is mapped onto a full  $T$ -period on the other side. If the topography has supercritical slopes on the plus side, then  $T_+$  consists of a part  $T_+'$  that is mapped onto  $T_-$  and a part  $T_+''$  that is mapped onto itself. This is the situation depicted in Fig. 2. If the topography has supercritical slopes on both sides, then  $T_+ = T_+' \cup T_+''$  and  $T_- = T_-' \cup T_-''$  such that  $T_+'$  is mapped onto  $T_-'$ ,  $T_+''$  onto itself,  $T_-'$  onto  $T_+'$  and  $T_-''$  onto itself.

Note that the explicit form of the mapping function depends on the choice of the  $T$ -periods. The mapping function shown in Fig. 2 exhibits discontinuities at  $\xi_1, \dots, \xi_5$ . Of these, the discontinuities at  $\xi_1, \xi_2$ , and  $\xi_4$  can be removed by choosing different  $T$ -periods. The discontinuities at  $\xi_3$  and  $\xi_5$  are not removable. They occur for characteristics that intersect the bottom at points where the slope is critical. The mapping  $\mathcal{M}$  depends on the frequency and on the profile of the topography. It is implicitly defined by

$$\mathcal{M}(\xi) = \xi \pm 2 \sum_i^N h(x_i)/c, \quad (11)$$

where  $x_i$  ( $i = 1, \dots, N$ ) are the intersections of the characteristics with the bottom. The plus sign must be used if the characteristic is traced forwardly and the minus sign if it is traced backwardly. The first derivative of the mapping function is given by

$$\frac{d\mathcal{M}}{d\xi} = \prod_{i=1}^N \frac{1 \pm h'(x_i)/c}{1 \mp h'(x_i)/c}, \quad (12)$$

where  $h' = dh/dx$ . If one introduces the mapping function into the periodicity condition (9), it takes the form

$$f(\xi) = f(\mathcal{M}(\xi)). \quad (13)$$

*c. Formal solution*

We now construct the formal solution. Consider again the situation depicted in Fig. 1. In the far fields, the bottom is flat with depths  $H_{\pm}$ . The half lengths of the  $T$ -periods in the far fields are

$$\gamma_{\pm} = \int_{-H_{\pm}}^0 \frac{dz}{c_0}. \quad (14)$$

An incident plane wave with modenumber  $n^i$  and amplitude  $a^i$  that propagates onto the topography from the plus side has the form

$$f_+^i(\xi) = a^i \exp\left(-i \frac{n^i \pi}{\gamma_+} \xi\right). \quad (15)$$

The sign in the exponent of (15) is chosen such that (15) represents an incoming wave with a group velocity or energy flux toward the topography. The complete wave field in the far fields is

$$f_+(\xi) = f_+^i(\xi) + f_+^s(\xi) \quad (16a)$$

$$f_-(\xi) = f_-^s(\xi), \quad (16b)$$

where  $f_{\pm}^s(\xi)$  is the backscattered or reflected field and  $f_{\pm}^i(\xi)$  the forwardscattered or transmitted field. If we substitute this representation into the periodicity condition (13), we obtain

$$f_+^s(\xi) + a^i \exp\left(-i \frac{n^i \pi}{\gamma_+} \xi\right) = \begin{cases} f_-^s(\mathcal{M}(\xi)) & \xi \in T'_+, \quad \mathcal{M}(\xi) \in T'_- \\ f_+^s(\mathcal{M}(\xi)) + a^i \exp\left(-i \frac{n^i \pi}{\gamma_+} \mathcal{M}(\xi)\right) & \xi \in T''_+, \quad \mathcal{M}(\xi) \in T''_+ \end{cases} \quad (17a)$$

$$f_-^s(\xi) = \begin{cases} f_+^s(\mathcal{M}(\xi)) + a^i \exp\left(-i \frac{n^i \pi}{\gamma_+} \mathcal{M}(\xi)\right) & \xi \in T'_-, \quad \mathcal{M}(\xi) \in T'_+ \\ f_-^s(\mathcal{M}(\xi)) & \xi \in T''_-, \quad \mathcal{M}(\xi) \in T''_- \end{cases} \quad (17b)$$

for the subintervals of the  $T$ -periods.

In the far field  $f_{\pm}^s(\xi)$  are periodic functions with periods  $2\gamma_{\pm}$ . They can thus be represented by Fourier series

$$f_{\pm}^s(\xi) = \sum_{n=0}^{\infty} a_n^{\pm} \exp\left(\pm i \frac{n\pi}{\gamma_{\pm}} \xi\right), \quad (18)$$

where the Fourier index  $n$  is also the modenumber. The coefficients for negative integers vanish since the radiation condition requires that the scattered field is an outgoing field with the group velocity or energy flux vector pointing away from the topography. The two constant terms  $a_0^+$  and  $a_0^-$  enter (17) only in the combination  $a_0^+ - a_0^-$ . We thus can set  $a_0^- = 0$  without loss of generality. If we substitute this Fourier representation into the periodicity condition (17) and project onto the  $m^{\text{th}}$  Fourier mode, we obtain the following set of equations

$$\sum_{n=0}^{\infty} (\delta_{nm} - A_{nm}) a_n^+ - \sum_{n=1}^{\infty} B_{nm} a_n^- = -a^i S_m^+, \quad m = 0, \dots, \infty \quad (19a)$$

$$\sum_{n=1}^{\infty} (\delta_{nm} - C_{nm}) a_n^- - \sum_{n=0}^{\infty} D_{nm} a_n^+ = -a^i S_m^-, \quad m = 1, \dots, \infty, \quad (19b)$$

where

$$A_{nm} = \frac{1}{T_+} \int_{T''_+} \exp\left(i \frac{n\pi}{\gamma_+} \mathcal{M}(\xi)\right) \exp\left(-i \frac{m\pi}{\gamma_+} \xi\right) d\xi$$

$$B_{nm} = \frac{1}{T_+} \int_{T'_+} \exp\left(-i \frac{n\pi}{\gamma_-} \mathcal{M}(\xi)\right) \exp\left(-i \frac{m\pi}{\gamma_+} \xi\right) d\xi$$

$$S_m^+ = \frac{1}{T_+} \int_{T''_+} \exp(-ik^i \mathcal{M}(\xi)) \exp\left(-i \frac{m\pi}{\gamma_+} \xi\right) d\xi$$

$$C_{nm} = \frac{1}{T_-} \int_{T''_-} \exp\left(-i \frac{n\pi}{\gamma_-} \mathcal{M}(\xi)\right) \exp\left(i \frac{m\pi}{\gamma_-} \xi\right) d\xi$$

$$D_{nm} = \frac{1}{T_-} \int_{T'_-} \exp\left(i \frac{n\pi}{\gamma_+} \mathcal{M}(\xi)\right) \exp\left(i \frac{m\pi}{\gamma_-} \xi\right) d\xi$$

$$S_m^- = \frac{1}{T_-} \int_{T'_-} \exp(-ik^i \mathcal{M}(\xi)) \exp\left(i \frac{m\pi}{\gamma_-} \xi\right) d\xi. \quad (20)$$

Equations (19) determine the modal amplitudes  $a_n^\pm$  of the forward- and backscattered field. The formal inversion of (19) yields

$$\alpha_n^\mu = a^i \sum_{\mu'=\pm} \sum_{n'=0}^{\infty} R_{nn'}^{\mu\mu'} S_n^{\mu'} \quad (21)$$

$$\mu = \pm, \quad n = 0, 1, 2, \dots,$$

where  $R_{nn'}^{\mu\mu'}$  is the (not explicitly known) inverse of the matrix operator constituting the left-hand side of (19).

The scattered field depends on the parameters of the incident wave and of the topography. The scattered field is proportional to the incident amplitude  $a^i$ . The horizontal wavenumber  $k^i = n^i \pi / \gamma_+$  of the incident wave enters through  $S_n^{\mu'}$ . The topography and the frequency enter both  $R_{nn'}^{\mu\mu'}$  and  $S_n^{\mu'}$  through the mapping function  $\mathcal{M}$ . If one introduces the nondimensional coordinates  $\tilde{x} = xc_0/H_0$  and  $\tilde{z} = z/H_0$ , the mapping function depends only on the scaled topography,

$$\tilde{z} = -h(\tilde{x}H_0/c_0)/H_0 = -\tilde{h}(\tilde{x}). \quad (22)$$

The most important parameters of the scaled topography are the relative height of the topography and the normalized slope  $h'(x)/c_0$ . Note that the scattering problem is reversible. If  $f_+^i(\xi)$  and  $f_-^s(\xi)$  is a solution, so is  $f_-^s(-\xi)$  and  $f_+^i(-\xi)$  consisting of wave fields  $f_-^s(-\xi)$  propagating toward the topography and a plane wave  $f_+^i(-\xi)$  propagating away from it.

Equation (19) is obtained by implementing the radiation condition that the scattered field must be an outgoing field. Reflection theory determines the scattered field by simply tracing the amplitude along characteristics,  $f(\xi) = f^i(\mathcal{M}(\xi))$ , or explicitly

$$f_+^s(\xi) = \begin{cases} 0 & \xi \in T'_+, \quad \mathcal{M}(\xi) \in T'_- \\ a^i \exp(-ik^i \mathcal{M}(\xi)) & \xi \in T''_+, \quad \mathcal{M}(\xi) \in T''_+ \end{cases} \quad (23a)$$

$$f_-^s(\xi) = \begin{cases} a^i \exp(-ik^i \mathcal{M}(\xi)) & \xi \in T'_-, \quad \mathcal{M}(\xi) \in T'_+ \\ 0 & \xi \in T''_-, \quad \mathcal{M}(\xi) \in T''_- \end{cases} \quad (23b)$$

The modal amplitudes can be obtained by Fourier transformation. Reflection theory has been used in earlier studies (e.g., Longuet-Higgins 1966). It does not satisfy the radiation condition. In section 5 we will compare the two solutions.

#### d. Energy flux

The wave equation (3) and the boundary condition (4) imply

$$\frac{d}{dx} F(x) = 0, \quad (24)$$

where

$$F(x) = \frac{\omega^2 - f^2}{4i\omega} \int_{-h(x)}^0 c_0^{-2} (\Psi^* \partial_x \Psi - \Psi \partial_x \Psi^*) dz. \quad (25)$$

With the formulas given in appendix A, it can be shown that

$$F(x) = \frac{1}{4} \int_{-h(x)}^0 (pu^* + p^*u) dz. \quad (26)$$

Thus,  $F(x)$  is the vertically integrated energy flux and (24) states that this flux is constant, that is, independent of  $x$ . This is a consequence of the conservation of energy for our problem.

If we express  $\Psi$  in terms of  $f$  and substitute the Fourier representation (18), the energy conservation law implies

$$\sum_{m=1}^{\infty} F_-^s(\omega, m) + \sum_{m=1}^{\infty} F_+^s(\omega, m) = F^i(\omega, n^i), \quad (27)$$

where

$$F(\omega, m) = \frac{\pi(\omega^2 - f^2)}{\omega} m a a^* \quad (28)$$

is the magnitude of the energy flux of a single plane wave of amplitude  $a$ , frequency  $\omega$ , and modenumber  $m$ . Equation (27) states that the incoming energy flux  $F^i(\omega, n^i)$  is only redistributed. It is partially transmitted and partially reflected and scattered to different modenumbers. This redistribution of the incoming energy flux will be our major diagnostic tool to describe the effect of scattering.

### 3. Analytical solutions

Larsen (1968) found an analytical solution for the scattering at a knife edge by matching a superposition of plane waves on both sides across the knife edge. Below we show that we can reproduce his results, which serves as a check on our derivation of (19). The analytical knife edge solution will also be used in section 4 to test the accuracy of our numerical solution technique. Bottom topographies for which the mapping function is linear also allow analytical solutions. These are the only cases known to us.

#### a. Knife edge

Consider a knife edge at  $x = 0$  of height  $d$  in an ocean of depth  $H$ . Choose the  $T$ -periods on the right and left side as

$$\left( \frac{H-d}{c_0}, \frac{3H-d}{c_0} \right) \quad \text{and} \quad \left( -\frac{3H-d}{c_0}, -\frac{H-d}{c_0} \right).$$

The mapping function then becomes

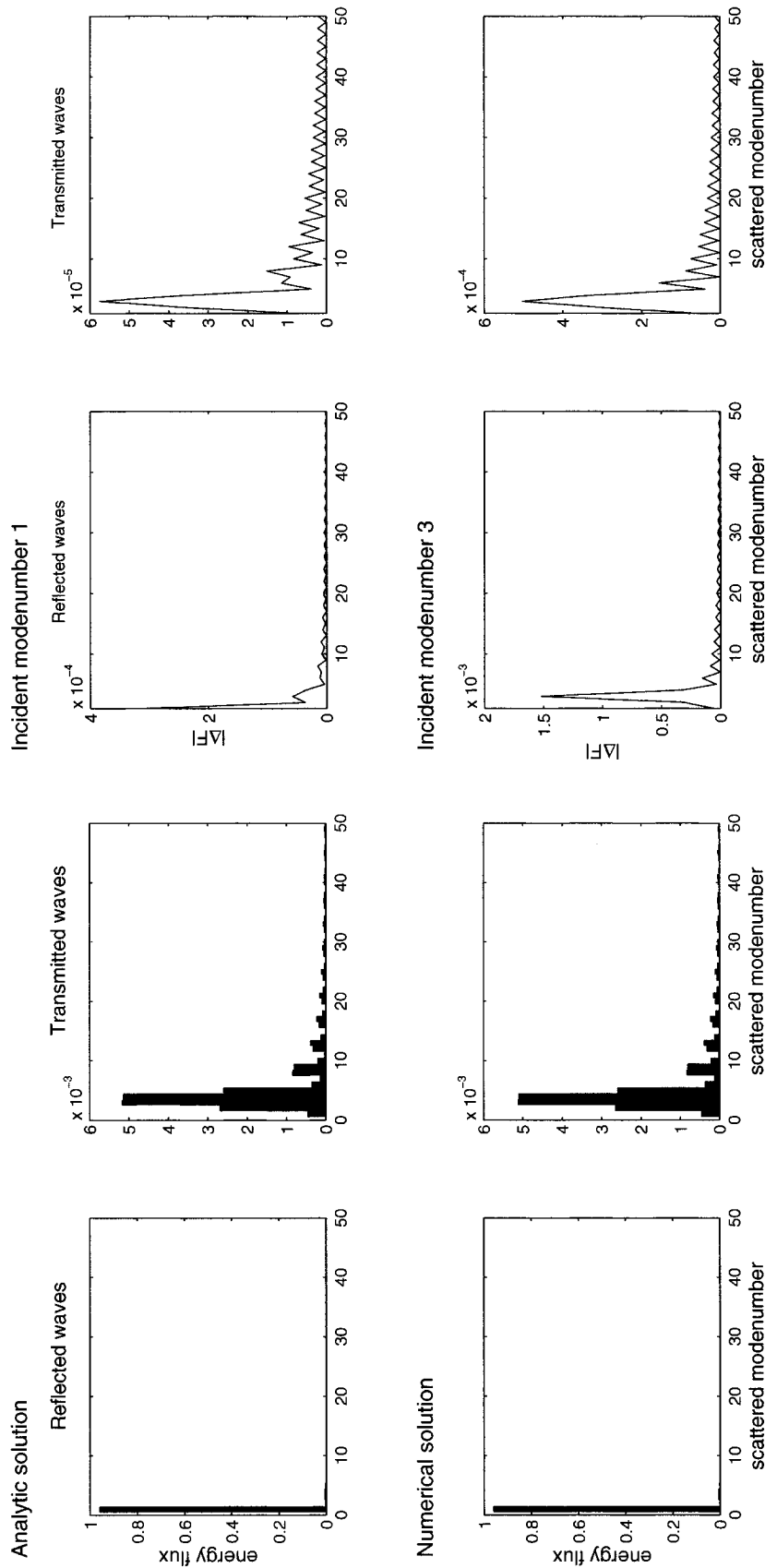


FIG. 3. Comparison of analytical and numerical solutions for a knife edge barrier. The distribution of the reflected and transmitted energy flux is given as a function of modenumber. Incident modenumber  $n^i = 1$ . Relative height of knife-edge barrier  $\tilde{d} = 0.25$ . Truncation modenumber  $M = 512$ .

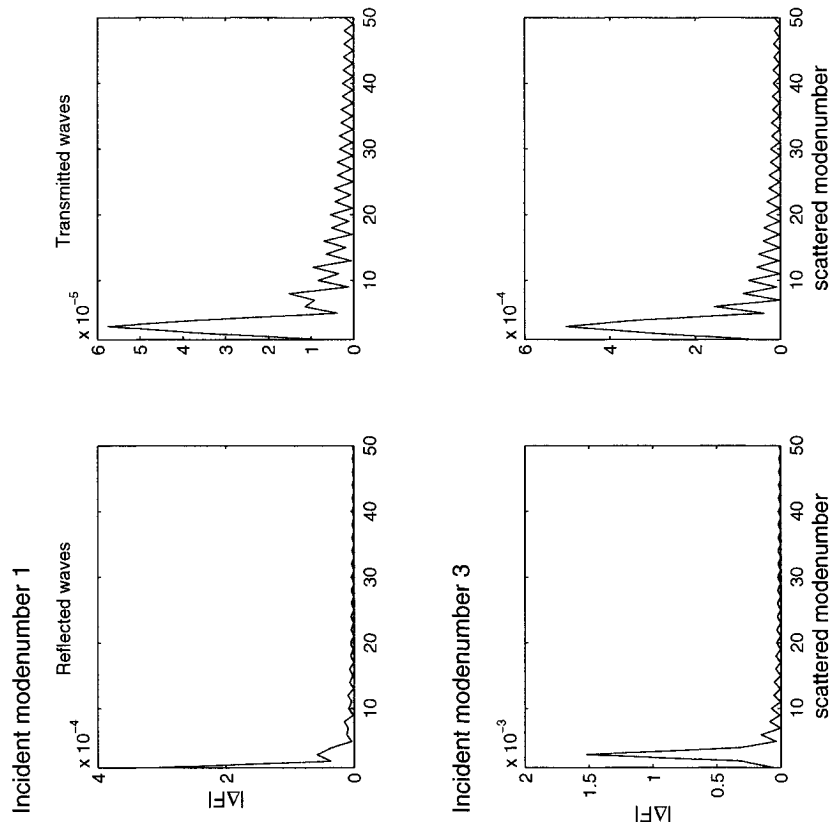


FIG. 4. Difference between analytical and numerical solutions for incident modenumber  $n^i = 1$  and 3. The flux difference is given as a function of modenumber for reflected and transmitted waves. Relative height of knife edge barrier  $\tilde{d} = 0.75$ . Truncation modenumber  $M = 512$ .

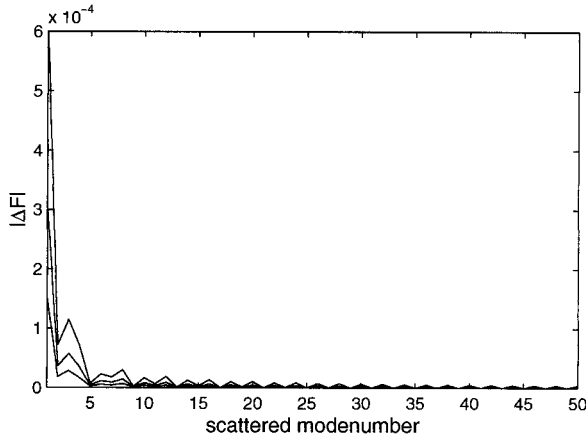


FIG. 5. Difference between analytical and numerical solutions for three different resolutions  $R = 4M$ ,  $8M$ , and  $16M$  with  $M = 256$ . The difference of the reflected energy fluxes is given as a function of modenumber. Relative height of knife edge barrier  $\tilde{d} = 0.75$ . Incident modenumber  $n^i = 1$ .

$$M(\xi) = \begin{cases} -\frac{4H}{c_0} + \xi & \xi \in T'_+ = \left(\frac{H+d}{c_0}, \frac{3H-d}{c_0}\right) \\ \frac{2H}{c_0} - \xi & \xi \in T''_+ = \left(\frac{H-d}{c_0}, \frac{H+d}{c_0}\right) \\ \frac{4H}{c_0} + \xi & \xi \in T'_- = \left(-\frac{3H-d}{c_0}, -\frac{H+d}{c_0}\right) \\ -\frac{2H}{c_0} - \xi & \xi \in T''_- = \left(-\frac{H+d}{c_0}, -\frac{H-d}{c_0}\right) \end{cases} \quad (29)$$

and the coefficients (20) become

$$\begin{aligned} A_{nm} &= C_{nm} = -B_{nm} = -D_{nm} \\ &= \frac{(-1)^{n+m}}{\pi(n+m)} \sin(n+m)\pi\tilde{d}, \quad n+m \neq 0 \\ A_{00} &= C_{00} = \tilde{d} \quad B_{00} = D_{00} = 1 - \tilde{d} \\ S_m^+ &= -S_m^- = \frac{(-1)^{n^i-m}}{\pi(n^i-m)} \sin(n^i-m)\pi\tilde{d}, \quad m \neq n^i \\ S_0^+ &= \tilde{d} \quad S_0^- = 1 - \tilde{d}, \end{aligned} \quad (30)$$

where  $\tilde{d} = d/H$ . With these coefficients, we find from (19)

$$a_n^+ + a_n^- = a^i \delta_{n,n^i} \quad n = 1, 2, 3, \dots \quad (31)$$

and

$$\begin{aligned} \sum_{n=1}^{\infty} a_n^+ \sin \frac{n\pi}{\gamma} \xi &= a^i \sin \frac{n^i \pi}{\gamma} \xi \quad \xi \in T''_+ \\ \sum_{n=0}^{\infty} a_n^+ \cos \frac{n\pi}{\gamma} \xi &= 0 \quad \xi \in T''_+. \end{aligned} \quad (32)$$

These equations are different but equivalent to Eqs.

(2.10) and (2.14) in Larsen (1968). For incident mode-number  $n^i = 1$ , the solution to (32) was derived by Larsen and is given by

$$\begin{aligned} \frac{a_1^+}{a_1^i} &= \sin^2(\tilde{d}\pi/2) - \frac{1}{2}P_2(\cos\tilde{d}\pi) \\ &+ \left(\frac{1}{2} - \sin^2(\tilde{d}\pi/2)\right)P_1(\cos\tilde{d}\pi) \\ \frac{na_n^+}{a_1^i} &= \sin^2(\tilde{d}\pi/2)[P_{n-1}(\cos\tilde{d}\pi) - P_n(\cos\tilde{d}\pi)] \\ &+ \frac{1}{2}[P_n(\cos\tilde{d}\pi) + P_{n-2}(\cos\tilde{d}\pi) - P_{n+1}(\cos\tilde{d}\pi) \\ &- P_{n-1}(\cos\tilde{d}\pi)] \quad \text{for } n > 1, \end{aligned} \quad (33)$$

where  $P_n$  are the Legendre polynomials. Using Larsen's solution technique, we also derived the solution for modenumbers  $n^i = 2$  and 3. They are given in appendix B.

Note that the solution depends only on the relative height  $\tilde{d} = d/H$  and is independent of the frequency  $\omega$  or the wave slope  $c_0$ . This is to be expected since  $\tilde{d}$  is the only parameter appearing in the scaled topography (22).

#### b. Linear mapping

Consider subcritical topography for which both  $T''_+$  and  $T''_-$  are null intervals and hence

$$A_{nm} = C_{nm} = S_m^+ = 0. \quad (34)$$

Furthermore, assume that the topography is of a form such that the mapping function is linear, say

$$M(\xi) = \begin{cases} c_1 + \frac{\gamma_-}{\gamma_+} \xi & \text{for } \xi \in T_+ \\ c_2 + \frac{\gamma_+}{\gamma_-} \xi & \text{for } \xi \in T_-, \end{cases} \quad (35)$$

where  $c_1$  and  $c_2$  are constants depending on the choice of the  $T$ -periods. Then

$$B_{nm} = D_{nm} = 0 \quad S_m^- = \delta_{n^i m}, \quad (36)$$

and hence

$$a_m^+ = 0 \quad a_m^- = \begin{cases} 0 & \text{for } m \neq n^i \\ a^i & \text{for } m = n^i. \end{cases} \quad (37)$$

The incident wave is fully transmitted and retains its modenumber. The vertical wavenumber will of course change if the ocean depths are different on the two sides of the topography, as in the slope-shelf configuration.

For a linear slope (or triangle ridge) the mapping function is linear if

$$2 \sum_{i=1}^{L-1} \left(\frac{\beta+1}{\beta-1}\right)^i + \alpha + 1 = \beta(\alpha-1), \quad (38)$$

where  $\alpha = H_+/H_-$ ,  $\beta = c_0/h'$ , and  $L = 1, 2, \dots$  is the number of times a characteristic intersects the slope before reaching the shelf (or the top of the ridge). For given topography (38) is a condition on  $\beta$  and hence on the wave slope  $c_0$  or the wave frequency  $\omega$ . A linear slope and a triangle ridge are transparent to waves with frequencies that satisfy (38). Specifically, we find

$$\beta = \frac{\alpha + 1}{\alpha - 1} \quad \text{for } L = 1$$

$$\beta = \frac{\alpha + 1}{\alpha - 1} + \sqrt{\left(\frac{\alpha + 1}{\alpha - 1}\right)^2 + 1} \quad \text{for } L = 2. \quad (39)$$

#### 4. Numerical method

To investigate other types of topography, we need to solve (19) numerically. This requires a number of steps. First, we numerically trace  $R$  characteristics from each  $T$ -period, either to the other  $T$ -period or onto itself. This tracing provides values of the mapping function  $\mathcal{M}(\xi)$  at  $2R$  discrete points. For our case studies we will choose  $R = 1024$  or  $2048$ . Second, we calculate the coefficients (20) for this mapping function using FFT algorithms. Third, we invert (19) by truncating the Fourier sum at a maximum modenumber  $M$ . Specifically, we use lower triangular and upper triangular matrix (LU) decomposition by Crout's method with implicit pivoting (Press et al. 1989). The truncation modenumber  $M$  can be chosen independently from the resolution  $R$ , except that it must be smaller than  $R$ . For our case studies we will always use  $M = R/4$ , that is,  $M = 256$  or  $512$ . To assess the performance of our numerical procedure we calculate the scattered modal amplitudes for a knife edge with  $\tilde{d} = 0.75$  and compare the numerical results to the analytical results of the previous section.

Figure 3 compares the reflected and the transmitted energy fluxes as a function of modenumber for an incident modenumber  $n^i = 1$ . Most of the energy flux is reflected. The numerical solution reproduces the analytical solution very well. The difference is shown in Fig. 4. The difference is of the order of  $10^{-4}$ . The largest difference occurs at the lowest modenumber, with the difference still being smaller than  $10^{-3}$ . The total reflected and transmitted energy fluxes are 0.9787 and 0.0212 from the numerical calculation and 0.9785 and 0.0214 from the analytical calculation. The differences for incident modenumber  $n^i = 3$  are similar (lower panel on Fig. 4). The numerical solutions also prove to be independent of frequency, with deviations of less than  $6 \times 10^{-6}$ . Numerical calculations for a step slope, the results of which should also be independent of frequency, gave similar relative deviations.

Figure 5 shows that the numerical solution rapidly converges to the analytical solution as the resolution is increased from  $R = 4M$  to  $R = 8M$  and  $R = 16M$  with the truncation modenumber held constant at  $M = 256$ . From this we conclude that our resolution of the map-

ping function is sufficient for the calculation of the coefficients (20).

The situation is different for the truncation modenumber  $M$ . Choosing  $M = 256$  or  $512$  is sufficient for the knife edge where the energy flux is scattered primarily to low modenumbers, smaller than  $M$ . This truncation modenumber, however, becomes insufficient when the topography contains critical or near-critical slopes and the energy flux is also scattered to modenumber larger than  $M$ . Since we are not interested in the detailed distribution of the scattered energy flux at high modenumbers, we keep the truncation modenumber at  $M = 256$  or  $512$ , even when the topography contains critical or near-critical slopes. In Part II we demonstrate that the amount of aliasing is tolerable. We can thus estimate the total energy flux scattered to the unresolved modenumbers as the difference between the incoming energy flux and the flux scattered to the resolved modenumbers.

There is also a physical reason for choosing a low truncation modenumber. Our theory only applies to low modenumbers that can propagate long distances before being affected by nonlinear and dissipative processes. High modenumber waves do not propagate far. They break, cause mixing, and dissipate. In Part II we calculate the energy flux scattered beyond a certain critical modenumber in order to assess the amount of internal wave energy available for mixing.

#### 5. Case studies

In order to understand the basic parameter dependencies, we numerically evaluate in this section the scattering of a single incident plane wave off the slope-shelf and ridge configurations listed in Table 1. In the slope-shelf configuration a flat shallow shelf is connected to a deep flat ocean by different slope profiles. The wave is incident from the ocean side. The ridge configurations are obtained by mirroring the slope-shelf configurations. Emphasis is on the slope-shelf configurations. The results for the ridge configurations are easily explainable in terms of the results for the slope-shelf configurations.

##### a. Parameter space

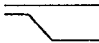
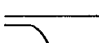
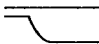
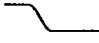
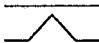



The incident wave is characterized by its modenumber  $n^i$  and by its frequency  $\omega$ . The topography is characterized by its height, its slope, and higher derivatives. As pointed out in section 2, the frequency and the topography enter the solution only through the scaled topography (22). For the slope-shelf configurations the basic parameters of the scaled topography are the depth ratio

$$\delta = \frac{H_-}{H_+} \quad (40)$$

and the normalized slope



TABLE 1. Topographic profiles for which numerical calculations have been performed. All cases were run for the eight depth ratios 1/32, 2/32, 4/32, 8/32, 12/32, 16/32, 20/32, and 24/32 and for 76 frequencies between  $f = 7.3 \times 10^{-5} \text{ s}^{-1}$  ( $\text{lat} = 30^\circ$ ) and  $\omega = 10f$ . The width of the topographic profiles is adjusted to keep the maximum slope at the given value. The resolution for all cases is  $R = 4M$ .

	Topography	Maximum slope	Truncation modenumber
	Linear slope	0.02	256 or 512
	Parabolic convex slope	0.04	256 or 512
	Parabolic concave slope	0.04	512
	Cosine slope	0.0314	512
	Triangular ridge	0.02	256 or 512
	Parabolic convex ridge	0.04	512
	Parabolic concave ridge	0.04	512
	Cosine ridge	0.0314	512

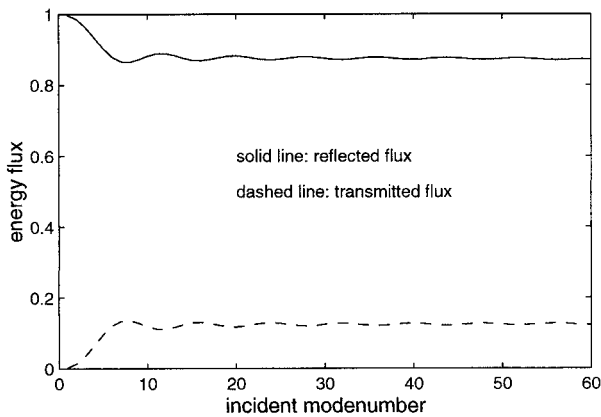


FIG. 6. Total reflected and transmitted energy flux as a function of incident modenumber for a supercritical linear slope. Depth ratio  $\delta = 1/8$ ; normalized slope  $\bar{s} = 1.715$ .

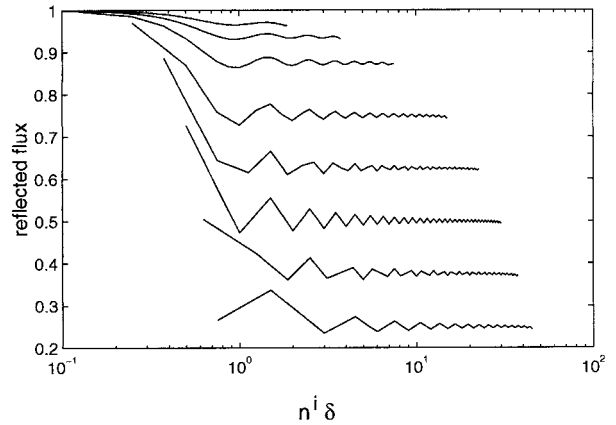


FIG. 7. Total reflected energy flux as a function of scaled incident modenumber  $n^i \delta$  for the eight depth ratios 1/32, 2/32, 4/32, 8/32, 12/32, 16/32, 20/32, and 24/32 (from top to bottom). Linear slope with supercritical slope  $\bar{s} = 1.715$ .

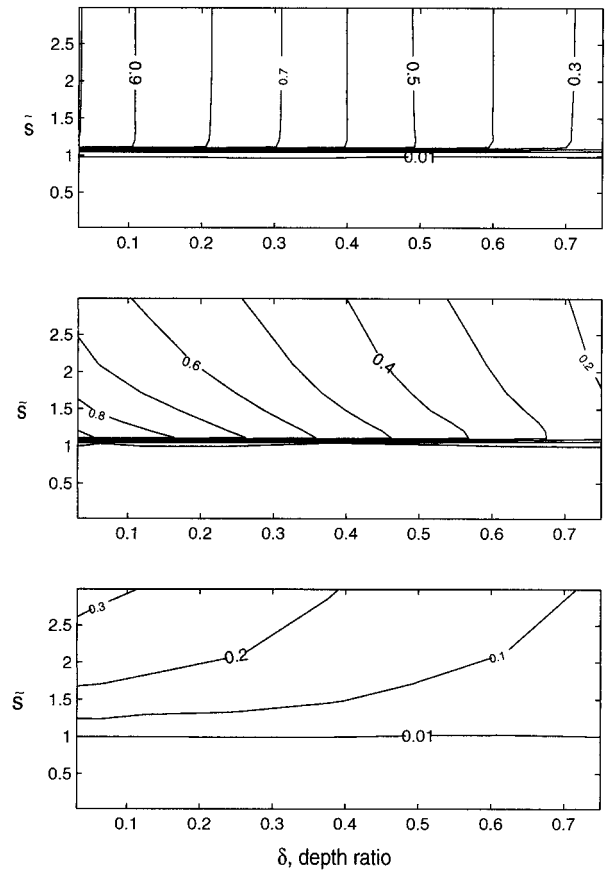


FIG. 8. Reflected energy flux as a function of depth ratio  $\delta$  and normalized slope  $\bar{s}$  for linear slope. Incident modenumber  $n^i = 10$ . Upper panel: Total reflected energy flux. Middle panel: energy flux reflected to modenumbers larger than the incident modenumber. Lower panel: energy flux reflected to modenumbers smaller than the incident modenumber.

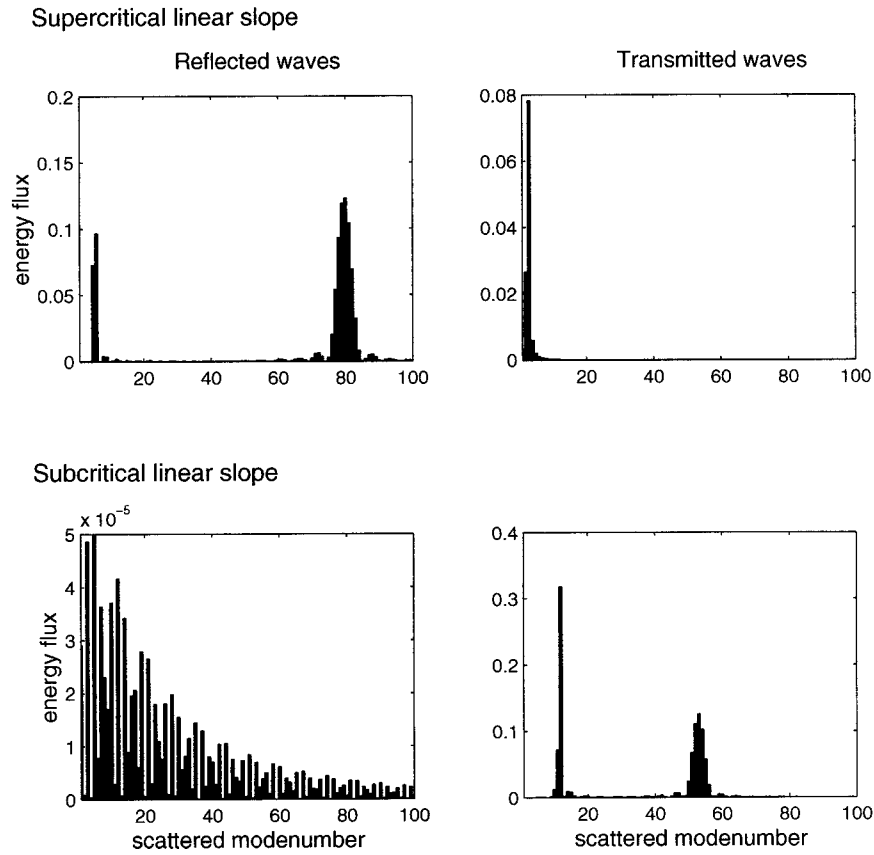


FIG. 9. Reflected and transmitted energy flux as a function of modenumber for a supercritical ( $\tilde{s} = 1.715$ ) and a subcritical ( $\tilde{s} = 0.636$ ) linear slope. Depth ratio  $\delta = 1/8$ . Incident modenumber  $n^i = 21$ .

$$\tilde{s} = \frac{h'}{c_0}. \tag{41}$$

When the maximum bottom slope exceeds the wave slope ( $\tilde{s}_{\max} > 1$ ), the topography is supercritical. For given topography this is the case for frequencies  $\omega$  smaller than the critical frequency

$$\omega_c = N^2 \frac{h_{\max}'^2}{1 + h_{\max}'^2} + f^2 \frac{1}{1 + h_{\max}'^2}. \tag{42}$$

For frequencies larger than  $\omega_c$  the topographic slope is smaller than the wave slope everywhere and the topography is subcritical. This distinction between sub- and supercritical topography is most important.

Our basic diagnostic tool is the redistribution of the incoming energy flux. We investigate how this redistribution depends on  $n^i$ ,  $\delta$ ,  $\tilde{s}$ , and some higher order characteristics of the topography. All energy fluxes are normalized by the incident energy flux.

*b. Linear slope*

In this case a linear slope connects a shelf of depth  $H_-$  to an ocean of depth  $H_+$ . For an infinite linear slope

the reflection law asserts that the wave is forward reflected if the slope is subcritical and backward reflected if the slope is supercritical. This remains largely true for a subcritical finite linear slope since all the characteristics from the deep ocean end up on the shelf. Ray tracing for a finite slope also suggests that not all of the incoming energy flux is backreflected for supercritical slopes, but that some of it is transmitted onto the shelf. This is indeed the case, as can be seen from Fig. 6 which shows the total reflected and transmitted energy flux as a function of incident modenumber. The reflected energy flux as a function of the scaled incident modenumber  $n^i \delta$  is shown in Fig. 7 for various depth ratios  $\delta$ . For low incident modenumbers,  $n\delta < 1$ , most of the energy flux is reflected. For high incident modenumbers,  $n\delta > 1$ , a fraction  $O(\delta)$  is transmitted and a fraction  $O(1 - \delta)$  is reflected. These fractions are nearly independent of  $\tilde{s}$ , except for near-critical slopes, as can be seen in Fig. 8. This figure also shows that most of the energy flux is reflected to higher modenumbers, especially for near critical slopes. This is a consequence of the fact that a unit length of slope receives more downward pointing rays that reflect to higher modenumbers than upward pointing rays that reflect to lower modenumbers.

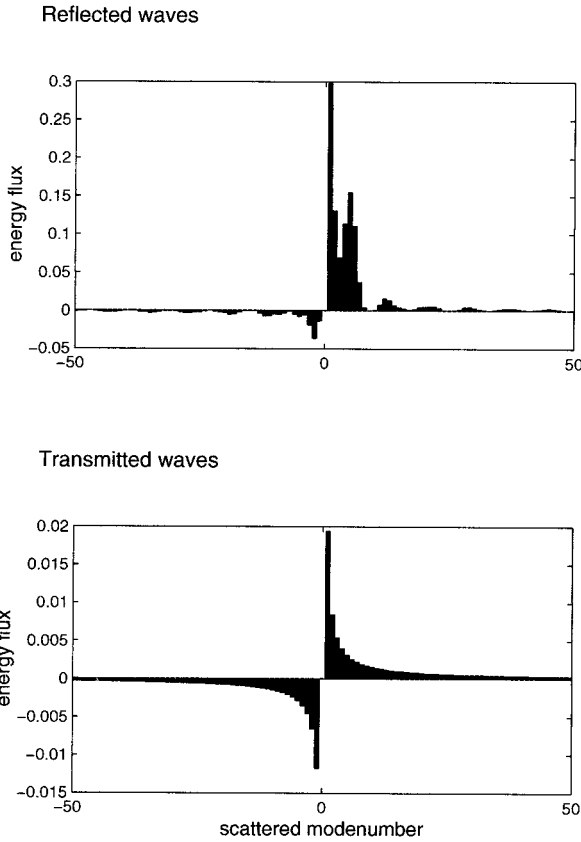


FIG. 10. “Reflected” and “transmitted” energy fluxes as a function of modenumber from reflection theory. Supercritical linear slope with  $\delta = 1/8$  and  $\bar{s} = 1.715$ . Incident modenumber  $n^i = 1$ .

The distribution of the reflected and transmitted energy flux in modenumber space is given in Fig. 9 for an incident modenumber  $n^i = 21$ , both for a super- and subcritical case. For the supercritical case, the reflected energy flux has peaks at

$$n_r^{(1)} = n^i \frac{\bar{s} - 1}{\bar{s} + 1} \tag{43a}$$

$$n_r^{(2)} = n^i \frac{\bar{s} + 1}{\bar{s} - 1}. \tag{43b}$$

These are the modenumbers predicted by the reflection laws for a wave propagating downward and upward onto an infinite slope. The transmitted waves have a peak at modenumber

$$n_t = n^i \delta \tag{44}$$

or at a vertical wavenumber that is the same as the one of the incident wave. This result is again expected from ray tracing where the transmitted waves are those whose rays do not intercept the slope.

For subcritical slopes, ray tracing implies peaks at

$$n_t = n^i \delta \left( \frac{\bar{s} + 1}{\bar{s} - 1} \right)^L, \tag{45}$$

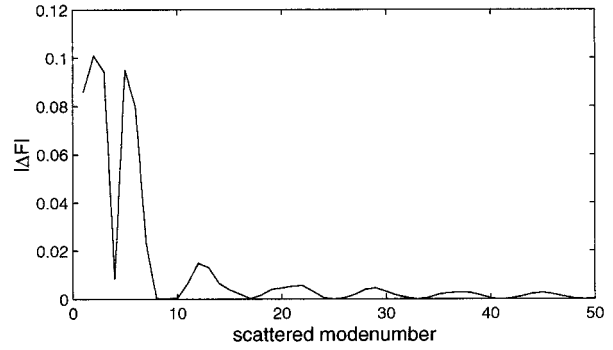


FIG. 11. Difference between scattering and reflection theory. The difference of the reflected energy fluxes is given as a function of modenumber. Supercritical slope with  $\delta = 1/8$  and  $\bar{s} = 1.715$ . Incident modenumber  $n^i = 1$ .

where  $L = 1, 2, \dots$  is the number of times that a ray intercepts the slope before it reaches the shelf. The  $L = 1, 2$  peaks can indeed be seen in Fig. 9. Overall, the scattering at a finite linear slope is largely explainable by ray tracing and application of reflection laws, especially for high incoming modenumbers.

*c. Comparison with reflection theory*

Reflection theory traces wave amplitudes along characteristics. The formal result is given by (23). One expects reflection theory to do the worst for low incident modenumbers. This is indeed the case. Figure 10 shows the distribution of the scattered energy flux at  $x = +\infty$  and  $x = -\infty$  as a function of modenumber for an incident modenumber  $n^i = 1$ . The topography is a supercritical linear slope. The energy flux at negative modenumbers is incident onto the topography, in violation of the radiation condition. This violation is especially pronounced for the “transmitted” energy flux at  $x = -\infty$  where nearly half of the flux is going in the wrong direction. However, the “reflected” energy flux at  $x = +\infty$  is also severely distorted as can be seen in Fig. 11 which shows the difference between the reflection and the scattering theory (for positive modenumbers only).

For subcritical topography, all characteristics are forwardly traced and reflection theory predicts no backscattering at all, in contrast to the scattering theory, where some of the incoming energy flux is backscattered.

Overall, the comparison suggests that it is important to implement the radiation conditions, especially for supercritical topography and low incident modenumbers.

*d. Staircase*

Bottom slopes are often represented by a series of steps, for numerical and other reasons. For example, Sjöberg and Stigebrandt (1992) use such a step topography to estimate the energy flux scattered from the

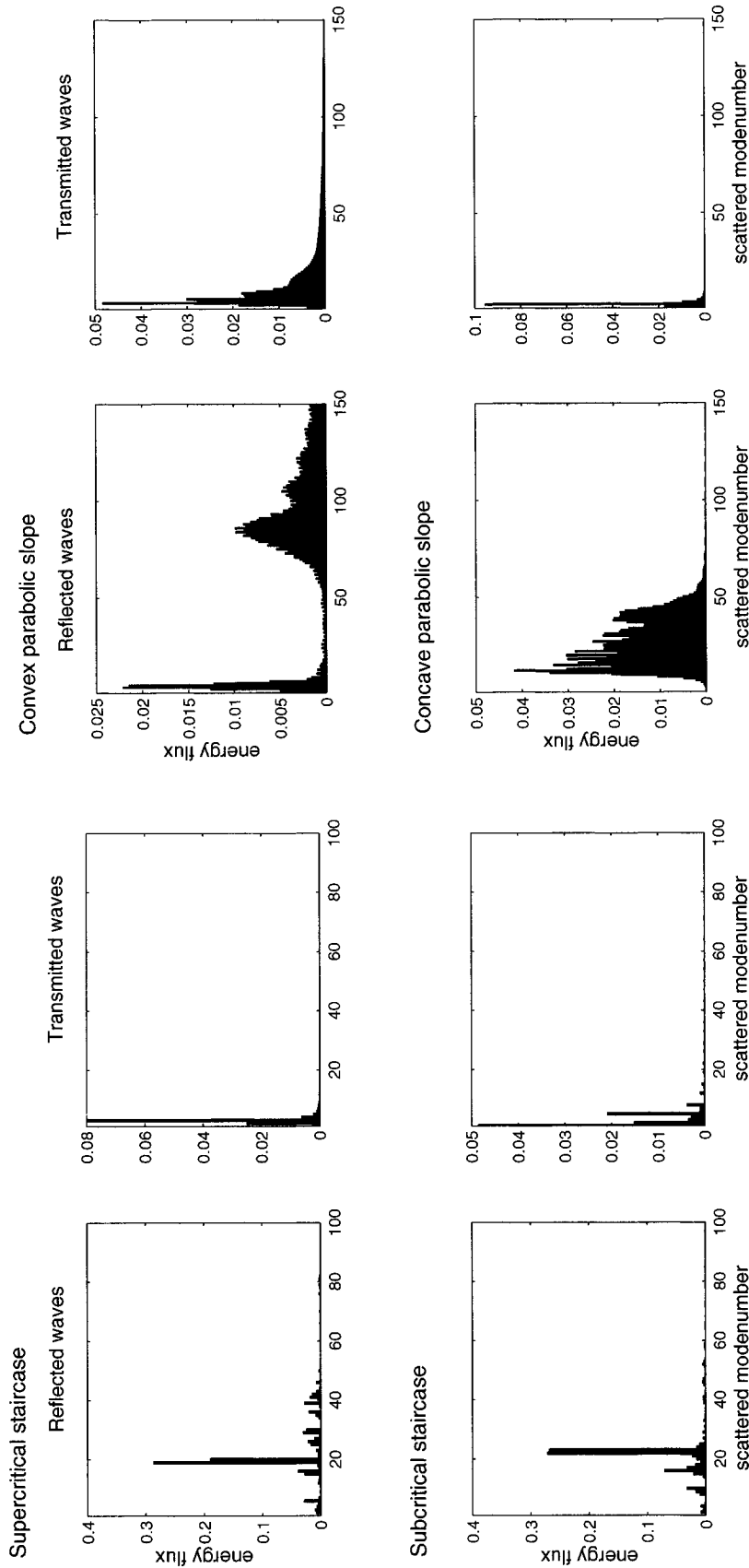


FIG. 12. Reflected and transmitted energy flux for a staircase with seven steps replacing the super- and subcritical linear slopes of Fig. 9. All other parameters are as in Fig. 9.

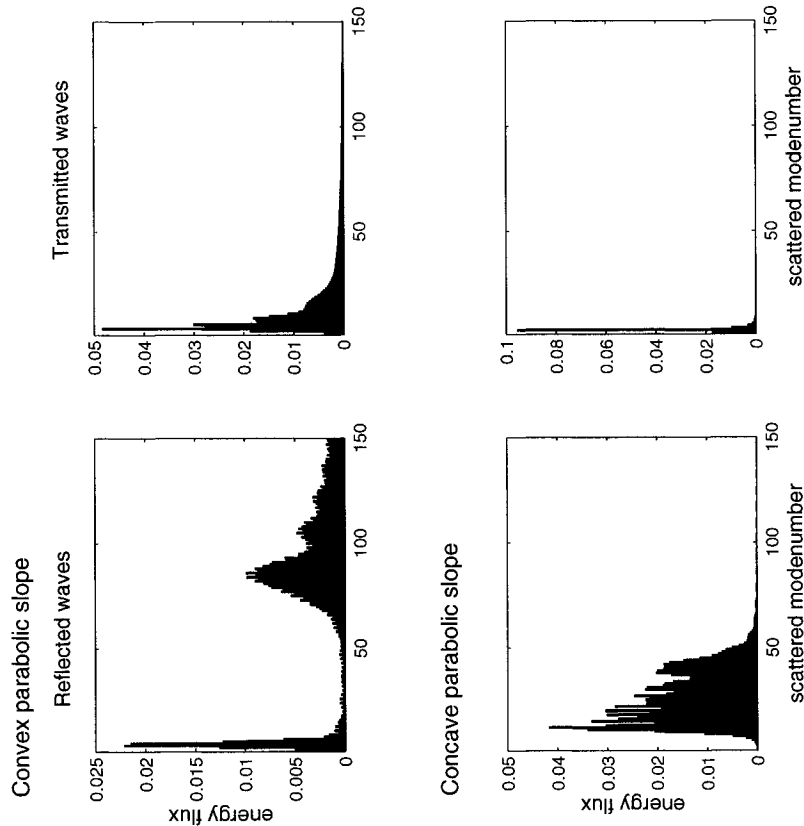


FIG. 13. Reflected and transmitted energy flux for supercritical convex and concave parabolic slope. Depth ratio  $\delta = 1/8$ . Maximum slope  $\hat{s} = 1.8457$ . Incident modenumber  $n' = 21$ .

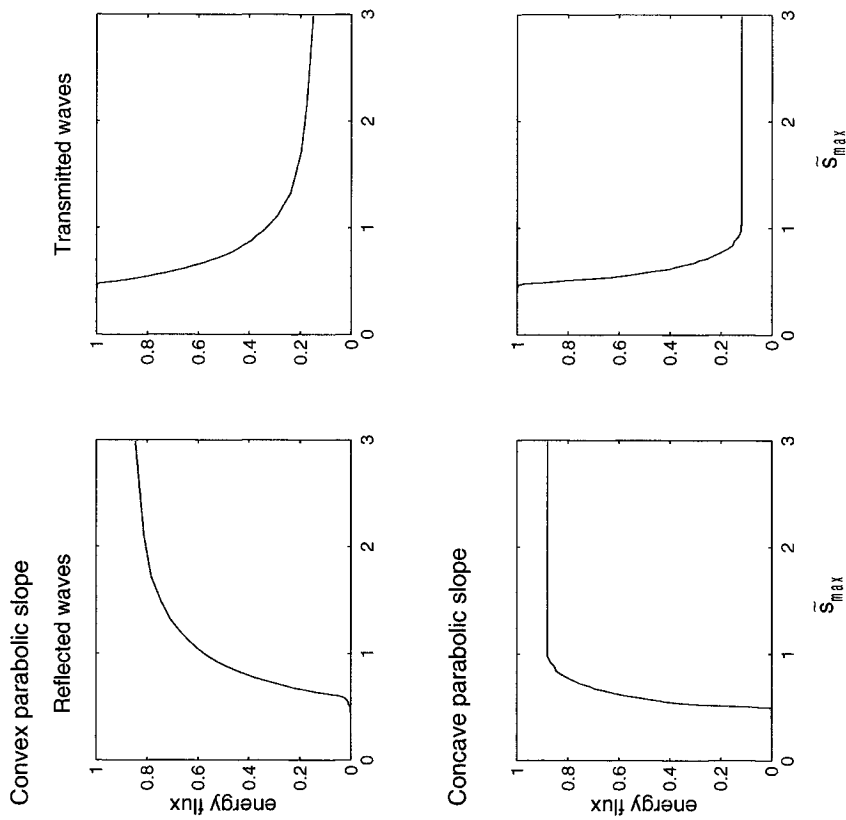


FIG. 14. Total reflected and transmitted energy flux as a function of maximum slope  $\bar{s}_{max}$  for convex and concave parabolic slope. Depth ratio  $\delta = 1/8$ . Incident modenumber  $n' = 21$ .

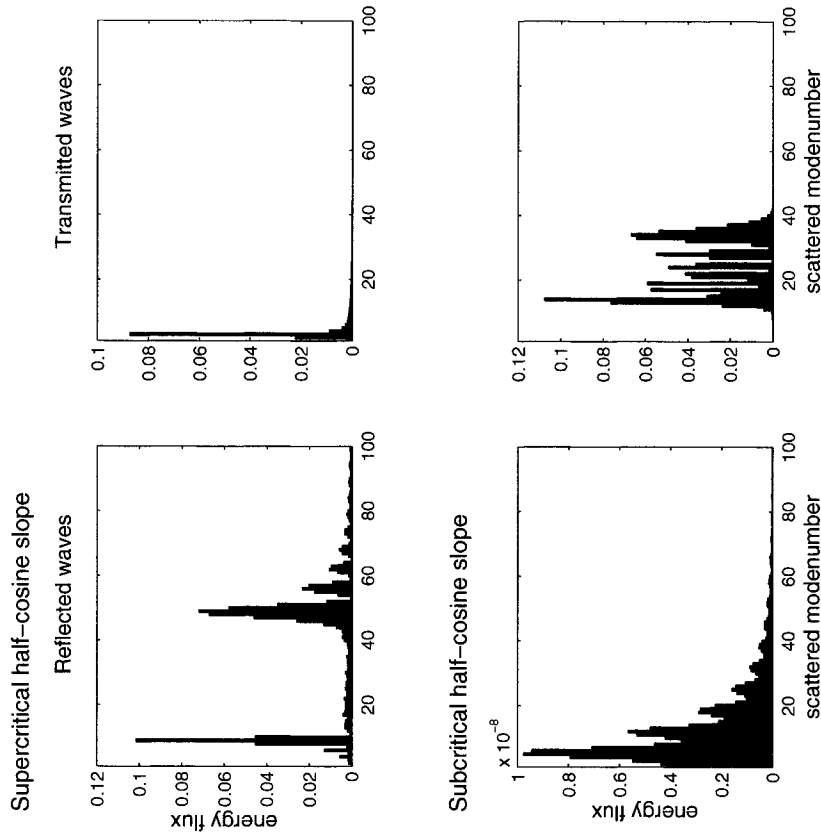


FIG. 15. Reflected and transmitted energy flux for a supercritical ( $\bar{s}_{max} = 1.694$ ) and subcritical ( $\bar{s}_{max} = 0.794$ ) half-cosine slope. Depth ratio  $\delta = 1/8$ . Incident modenumber  $n' = 21$ .

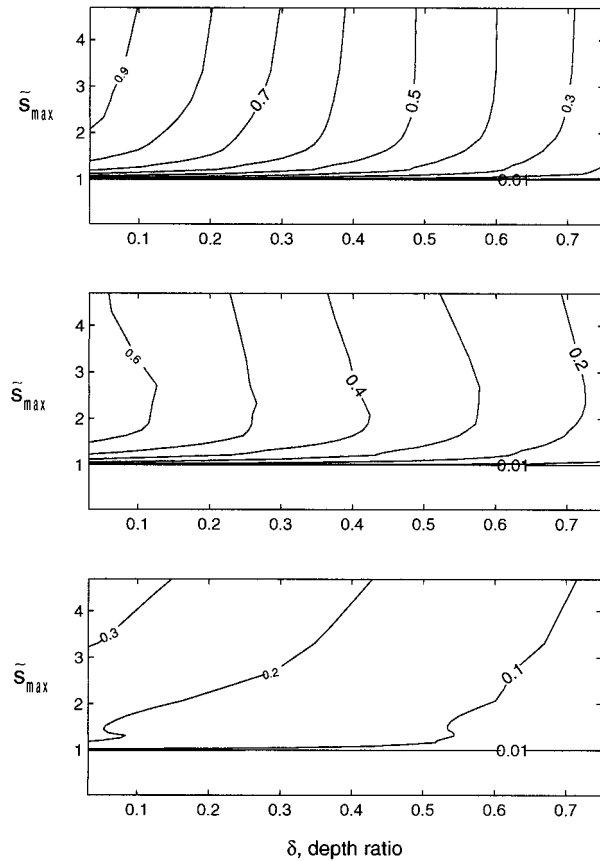


FIG. 16. Reflected energy flux as a function of depth ratio  $\delta$  and normalized slope  $\tilde{s}_{\max}$  for half-cosine slope. Incident modenumber  $n^i = 10$ . Upper panel: Total reflected energy flux. Middle panel: energy flux reflected to modenumbers larger than the incident modenumber. Lower panel: energy flux reflected to modenumbers smaller than the incident modenumber.

surface tide into internal tides. To assess the involved errors we replace the sub- and supercritical linear slopes of Fig. 9 by seven steps. The result is shown in Fig. 12 and bears little resemblance to the linear slope calculations of Fig. 9. For both the super- and subcritical case, the reflected energy becomes clustered around the incident modenumber  $n^i = 21$ . Furthermore, the total reflected energy flux for the subcritical case becomes comparable to the one for the supercritical case, in sharp contrast to the linear slope calculation in Fig. 9. This is to be expected. When a subcritical linear slope is replaced by a series of steps, the topography becomes supercritical along part of the slope. In the supercritical case, the differences become less dramatic for lower incident modenumbers because long waves feel the local structure of the topography less than short waves do.

*e. Convex versus concave*

Baines (1974) analyzed the scattering of an internal wave propagating downward onto supercritical topography and showed that convex topography is more ef-

ficient than concave topography in scattering energy to high wavenumbers. The reason is that for concave topography a near critical reflection is followed and partially cancelled by a subsequent near critical reflection. This quantitative difference between a convex and a concave slope remains valid for our finite depth ocean. Formally, it shows up in the derivative of the mapping function [see Eq. (12)]. For convex slopes it is singular at critical points. For concave slopes it remains regular. Here we analyze the difference in more detail using parabolic profiles. In the convex case it starts with zero slope at the shelf edge and has its largest slope (and a sharp corner) at the ocean edge. The concave profile starts with zero slope at the ocean edge and has its largest slope (and a sharp corner) at the shelf edge.

In the supercritical case, that is, in the case that the maximum slope exceeds the wave slope, the results for the convex and concave slopes are significantly different, as can be seen in Fig. 13 which shows the reflected and transmitted energy fluxes as a function of mode-number for an incident modenumber  $n^i = 21$ . Clearly more energy is scattered to higher modenumbers in the convex case than in the concave case. The total energy flux scattered to modenumbers larger than  $n = 100$  is 0.0695 for the convex slope and only 0.001 for the concave slope. Comparison with Fig. 9 shows that the energy flux distribution for the convex slope is similar to the one for the linear slope, although the peaks are much broader. Such broadening is expected because the local reflecting slope changes continuously for convex (and concave) topography. The results for the concave slope differ from those for the linear slope, and they also depend strongly on  $\tilde{s}_{\max}$ . As  $\tilde{s}_{\max} \rightarrow 1$  the distribution of the reflected energy flux tends to concentrate near the incident modenumber (not shown).

Another significant difference between convex and concave slopes is the partition into reflected and transmitted energy flux. Figure 14 shows the total amounts as a function of  $\tilde{s}_{\max}$ . For supercritical slopes, especially as one approaches the critical slope  $\tilde{s}_{\max} = 1$ , the concave slope is more effective than a convex slope in reflecting the incident energy flux backward. This is to be expected. The length of the slope that intercepts backward reflecting rays is larger for a concave than for a convex slope. For subcritical slopes the distribution in mode-number space is almost identical for the convex and concave slopes and broader than for the linear slope (not shown).

*f. Half-cosine slope*

The slope profiles considered so far all had slopes that were either constant or monotonic, leading to sharp corners where the slope meets the deep ocean or shelf. At these points the first derivative of the mapping function becomes discontinuous. The effect of these discontinuities is not very pronounced for supercritical slopes, where the critical points determine the behavior,

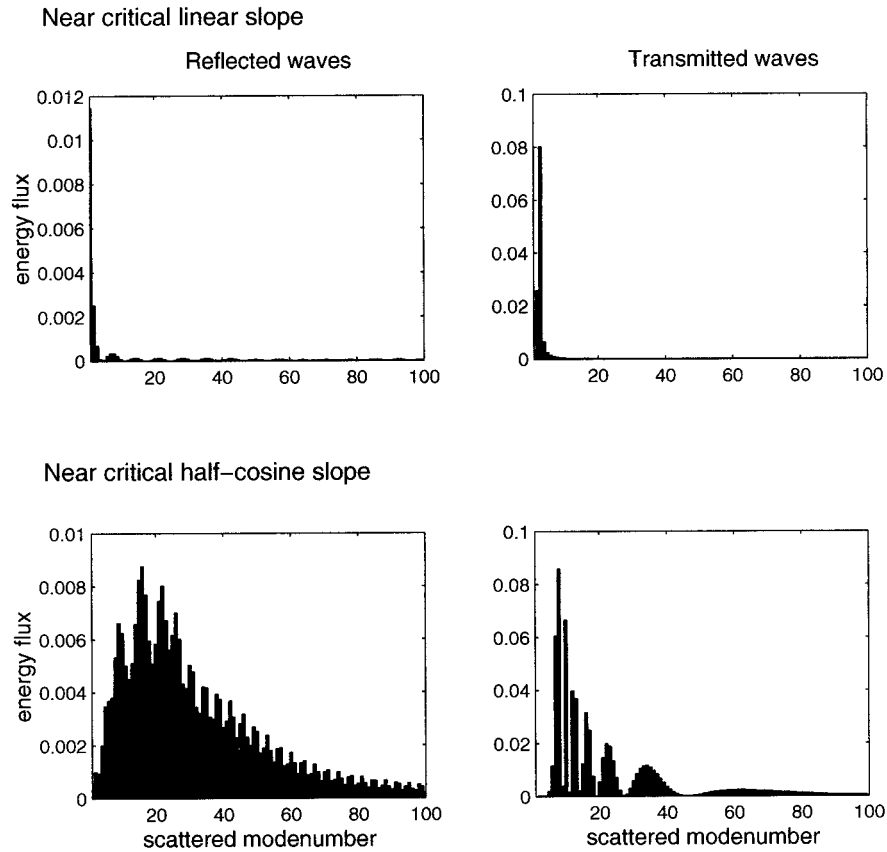


FIG. 17. Reflected and transmitted energy flux for near critical linear ( $\bar{s} = 1.037$ ) and near critical half-cosine ( $\bar{s}_{\max} = 1.0274$ ) slope. Depth ratio  $\delta = 1/8$ . Incident modenumber  $n^i = 21$ .

but exert influence for subcritical slopes. In this section we consider half-cosine slopes that provide a smooth transition from the shelf to the ocean. They have both a convex and a concave part. The maximum slope is midway.

Figure 15 shows the distribution of the reflected and transmitted energy flux as a function of modenumber for an incident modenumber  $n^i = 21$ , both for a super- and subcritical maximum slope. In the supercritical case, the distributions are very similar to the linear slope case. The location of the peaks is still given by the reflection laws (43), using the maximum slope (at the point of maximum slope, the curvature is zero and thus best approximated by a linear slope). For the subcritical case, the reflected energy flux is much less than for all the previously considered slope profiles. This is due to the removal of the sharp corners. Corners (and other abrupt changes) can have pronounced effects on internal wave scattering.

Figure 16 shows the dependence of the total reflected energy flux on the topographic parameters and its partition into the flux scattered to modenumbers higher and lower than the incident modenumber. It looks similar to the linear slope case shown in Figure 8, except that the transition from super- to subcritical slope is much more

gentle. This is to be expected since only points of the half-cosine slope approach the critical value and not the whole length of the slope as in the linear slope case. This difference also causes the distribution with modenumber to look very different for near-critical slopes. Figure 17 shows such a comparison for a near-critical linear slope and a near-critical half-cosine slope. The most dramatic difference is the part of the energy flux scattered to resolved modenumbers. It is only 0.1502 for the linear slope case and 0.9568 for the half-cosine slope.

#### g. Ridge configurations

The ridge configurations are obtained by mirroring the slope-shelf profiles. The depth ratio is now given by

$$\delta = \frac{H_+ - d}{H_+}, \quad (46)$$

where  $d$  is the height of the ridge. The partition into transmitted and reflected waves remains the same, that is, nearly all of the incoming flux is transmitted across the ridge for subcritical topography whereas a fraction  $O(\delta)$  is transmitted and a fraction  $O(1 - \delta)$  is reflected

for supercritical topography. The distribution in mode-number space also does not change for the reflected waves. These results are expected because they do not depend on the structure of the topography beyond its top. The distributions for the transmitted waves can also be inferred from the corresponding slope–shelf distributions. In the supercritical case, the distribution shows a broadened peak at the incident modenumber  $n^i$  rather than at  $n^i\delta$  as in the slope–shelf case. This is a geometric effect, solely due to the different depths on the minus side. The characteristics do not intercept the topography beyond the top of the ridge. Similarly, the distribution in the subcritical case can be obtained by expanding the modenumber axis by a factor  $\delta^{-1}$ .

In Part II we will consider the oceanographically more relevant case of waves incident from both sides onto the ridge.

## 6. Summary and conclusions

We derived a formal solution for the scattering of internal waves at finite topography in two dimensions and developed a numerical code for its numerical evaluation. The performance of the code was tested against the analytical solution for a knife edge barrier. We numerically calculated the scattering of a single plane wave incident on various slope–shelf and ridge configurations in order to understand the basic parameter dependences of the scattering process. Our diagnostic tool was the partition of the incident energy flux into transmitted and reflected flux and its redistribution in mode-number space.

The incident wave is characterized by its modenumber and frequency, the topography by its height, slope, and higher derivatives; the most important parameter is the ratio of bottom to wave slope. Scattering at supercritical topography is very different from scattering at subcritical topography. For subcritical topography nearly all of the incident wave energy flux is transmitted. For supercritical topography it is partly reflected and partly transmitted. The partition depends on the incident modenumber and the depth ratio of the topography. The distribution of the scattered energy flux in modenumber space also depends on slope, depth ratio, and incident modenumber. Most of the reflected energy is scattered to modenumbers higher than the incident modenumber.

Higher order derivatives of the topography are also important. A convex slope is much more efficient in scattering the incoming energy flux to higher modenumbers than a concave slope, and a linear slope is more efficient than a curved slope. Abrupt changes in the topography, such as sharp corners, also affect the scattering, especially for subcritical topography.

Reflection theory works well for incident waves whose wavelengths are smaller than the radius of curvature of the topography. In these cases, reflection theory correctly predicts the locations of the peaks in mode-

number space and the scattering to higher modenumbers for near-critical slopes. However, as the incident modenumber decreases, predictions from reflection theory become less and less accurate and must be replaced by solving the full scattering problem.

Because of the complex parameter dependence of the scattering problem, care must be taken when replacing rugged topography by smooth topography, curved topography by (piecewise) linear slopes, and linear slopes by a series of steps.

In Part II, we will consider a superposition of incident waves with a realistic spectrum, calculate not only the redistribution of the energy flux but also the energy and shear of the scattered wave field, and explore the implications for internal wave induced boundary mixing.

*Acknowledgments.* This work was supported by the Office of Naval Research.

## APPENDIX A

### Internal Wave Kinematics

Linear internal waves obey

$$\partial_t u - fv = -\partial_x p \quad (\text{A1a})$$

$$\partial_t v + fu = -\partial_y p \quad (\text{A1b})$$

$$\partial_t w = -\partial_z p - N^2 \zeta \quad (\text{A1c})$$

$$\partial_t \zeta = w \quad (\text{A1d})$$

$$\partial_x u + \partial_y v + \partial_z w = 0, \quad (\text{A1e})$$

where  $u$ ,  $v$ , and  $w$  are the three velocity components,  $p$  the pressure, and  $\zeta$  the vertical displacement. Equations (A1) imply the internal wave equation

$$(\partial_{tt} + N^2)(\partial_{xx} + \partial_{yy})p + (\partial_{tt} + f^2)\partial_{zz}p = 0. \quad (\text{A2})$$

For monochromatic waves of frequency  $\omega$  this reduces to

$$(\partial_{xx} + \partial_{yy})p - c^2 \partial_{zz}p = 0, \quad (\text{A3})$$

with  $c^2 = (\omega^2 - f^2)/(N^2 - \omega^2)$ . The other variables are given by

$$u = \frac{1}{\omega^2 - f^2} [(-i\omega \partial_x + f \partial_y)p] \quad (\text{A4a})$$

$$v = \frac{1}{\omega^2 - f^2} [(-i\omega \partial_y + f \partial_x)p] \quad (\text{A4b})$$

$$w = \frac{1}{N^2 - \omega^2} i\omega \partial_z p \quad (\text{A4c})$$

$$\zeta = -\frac{1}{N^2 - \omega^2} \partial_z p. \quad (\text{A4d})$$

For two-dimensional waves, with streamfunction  $\psi$ , the wave equation reduces to

$$\partial_{xx} \psi - c^2 \partial_{zz} \psi = 0, \quad (\text{A5})$$



and the internal wave variables are given by

$$u = \partial_z \psi \quad (\text{A6a}) \quad u = \frac{1}{\sqrt{c}} [f'(\xi) - g'(\eta)] \quad (\text{A7a})$$

$$v = -\frac{f}{\omega} \partial_z \psi \quad (\text{A6b}) \quad v = -\frac{f}{\omega \sqrt{c}} [f'(\xi) - g'(\eta)] \quad (\text{A7b})$$

$$w = -\partial_x \psi \quad (\text{A6c}) \quad w = -\sqrt{c} [f'(\xi) + g'(\eta)] \quad (\text{A7c})$$

$$\zeta = -\frac{i}{\omega} \partial_x \psi \quad (\text{A6d}) \quad \zeta = -\frac{i}{\omega} \sqrt{c} [f'(\xi) + g'(\eta)] \quad (\text{A7d})$$

$$\partial_x p = -\frac{\omega^2 - f^2}{i\omega} \partial_z \psi \quad (\text{A6e}) \quad p = -\frac{\omega^2 - f^2}{i\omega \sqrt{c}} [f(\xi) - g(\eta)]. \quad (\text{A7e})$$

If  $\psi = \sqrt{c} [f(\xi) + g(\eta)]$ , then

## APPENDIX B

### Knife Edge Solutions for $n^i = 2$ and 3

For  $n^i = 2$ ,

$$\frac{a_1^+}{2a^i} = c_1 [P_1(\cos \tilde{d}\pi) + P_2(\cos \tilde{d}\pi) - P_3(\cos \tilde{d}\pi) - 1] + c_2 [P_1(\cos \tilde{d}\pi) - P_2(\cos \tilde{d}\pi)] + c_3 [1 - P_1(\cos \tilde{d}\pi)]$$

$$\frac{a_2^+}{a^i} = c_1 [P_3(\cos \tilde{d}\pi) - P_4(\cos \tilde{d}\pi)] + c_2 [P_2(\cos \tilde{d}\pi) - P_1(\cos \tilde{d}\pi) - P_3(\cos \tilde{d}\pi) + 1] + c_3 [P_1(\cos \tilde{d}\pi) - P_2(\cos \tilde{d}\pi)]$$

$$\begin{aligned} \frac{na_n^+}{2a^i} &= c_1 [P_{n+1}(\cos \tilde{d}\pi) + P_{n-3}(\cos \tilde{d}\pi) - P_{n+2}(\cos \tilde{d}\pi) - P_{n-2}(\cos \tilde{d}\pi)] \\ &+ c_2 [P_n(\cos \tilde{d}\pi) + P_{n+2}(\cos \tilde{d}\pi) - P_{n+1}(\cos \tilde{d}\pi) - P_{n-1}(\cos \tilde{d}\pi)] + c_3 [P_{n-1}(\cos \tilde{d}\pi) - P_n(\cos \tilde{d}\pi)] \\ &\text{for } n > 2. \end{aligned} \quad (\text{B1})$$

For  $n^i = 3$ :

$$\begin{aligned} \frac{a_1^+}{3a^i} &= c_1 [P_3(\cos \tilde{d}\pi) + P_2(\cos \tilde{d}\pi) - P_4(\cos \tilde{d}\pi) - P_1(\cos \tilde{d}\pi)] \\ &+ c_2 [P_1(\cos \tilde{d}\pi) + P_2(\cos \tilde{d}\pi) - P_3(\cos \tilde{d}\pi) - 1] + c_3 [P_1(\cos \tilde{d}\pi) - P_2(\cos \tilde{d}\pi)] + c_4 [1 - P_1(\cos \tilde{d}\pi)] \end{aligned}$$

$$\begin{aligned} \frac{2a_2^+}{3a^i} &= c_1 [P_1(\cos \tilde{d}\pi) + P_4(\cos \tilde{d}\pi) - P_5(\cos \tilde{d}\pi) - 1] + c_2 [P_3(\cos \tilde{d}\pi) - P_4(\cos \tilde{d}\pi)] \\ &+ c_3 [1 + P_2(\cos \tilde{d}\pi) - P_1(\cos \tilde{d}\pi) - P_3(\cos \tilde{d}\pi)] + c_4 [P_1(\cos \tilde{d}\pi) - P_2(\cos \tilde{d}\pi)] \end{aligned}$$

$$\begin{aligned} \frac{a_3^+}{a^i} &= c_1 [P_5(\cos \tilde{d}\pi) - P_6(\cos \tilde{d}\pi)] + c_2 [1 + P_4(\cos \tilde{d}\pi) - P_1(\cos \tilde{d}\pi) - P_5(\cos \tilde{d}\pi)] \\ &+ c_3 [P_1(\cos \tilde{d}\pi) + P_3(\cos \tilde{d}\pi) - P_2(\cos \tilde{d}\pi) - P_4(\cos \tilde{d}\pi)] + c_4 [P_2(\cos \tilde{d}\pi) - P_3(\cos \tilde{d}\pi)] \end{aligned}$$

$$\begin{aligned} \frac{na_n^+}{3a^i} &= c_1 [P_{n+2}(\cos \tilde{d}\pi) + P_{n-4}(\cos \tilde{d}\pi) - P_{n+3}(\cos \tilde{d}\pi) - P_{n-3}(\cos \tilde{d}\pi)] \\ &+ c_2 [P_{n+1}(\cos \tilde{d}\pi) + P_{n-3}(\cos \tilde{d}\pi) - P_{n+2}(\cos \tilde{d}\pi) - P_{n-2}(\cos \tilde{d}\pi)] \\ &+ c_3 [P_{n-2}(\cos \tilde{d}\pi) + P_n(\cos \tilde{d}\pi) - P_{n+1}(\cos \tilde{d}\pi) - P_{n-1}(\cos \tilde{d}\pi)] + c_4 [P_{n-1}(\cos \tilde{d}\pi) - P_n(\cos \tilde{d}\pi)] \\ &\text{for } n > 3, \end{aligned} \quad (\text{B2})$$

where

$$\begin{aligned}
 c_1 &= \frac{1}{2} & c_2 &= \frac{1}{2}(1 - \cos\tilde{d}\pi) & c_3 &= \frac{1}{4}[3 - 2\cos\tilde{d}\pi - \cos^2\tilde{d}\pi] \\
 c_4 &= \frac{1}{4}(3 - \cos\tilde{d}\pi - \cos^2\tilde{d}\pi - \cos^3\tilde{d}\pi).
 \end{aligned}
 \tag{B3}$$

The transmitted wave amplitudes  $a_n^-$  can be determined from  $a_n^+$  by

$$a_n^- = -a_n^+ \quad \text{for } n \neq n^i \quad a_{n^i}^- = 1 - a_{n^i}^+. \tag{B4}$$

#### REFERENCES

- Baines, P. G., 1971a: The reflexion of internal/inertial waves from bumpy surfaces. *J. Fluid Mech.*, **46**, 273–291.
- , 1971b: The reflexion of internal/inertial waves from bumpy surfaces. Part 2: Split reflexion and diffraction. *J. Fluid Mech.*, **49**, 113–131.
- , 1973: The generation of internal tides by flat bumpy topography. *Deep-Sea Res.*, **20**, 179–205.
- , 1974: The generation of internal tides over steep continental slopes. *Philos. Trans. Roy. Soc. London*, **A277**, 27–58.
- , 1982: On internal tide generation models. *Deep-Sea Res.*, **29**, 307–338.
- Cox, C., and H. Sandstrom, 1962: Coupling of internal and surface waves in water of variable depth. *J. Oceanogr. Soc. Japan*, 20th Anniversary Volume, 499–513.
- Eriksen, C. C., 1982: Observations of internal wave reflection off sloping bottoms. *J. Geophys. Res.*, **87**, 525–538.
- Larsen, L. H., 1969: Internal wave incident upon a knife edge barrier. *Deep-Sea Res.*, **16**, 411–419.
- Longuet-Higgins, M. S., 1966: On the reflexion of wave characteristics from rough surface. *J. Fluid Mech.*, **37**, 231–250.
- Müller, P., and N. Xu, 1992: Scattering of oceanic internal gravity waves off random bottom topography. *J. Phys. Oceanogr.*, **22**, 474–488.
- , and X. Liu, 2000: Scattering of internal waves at finite topography in two dimensions. Part II: Spectral calculations and boundary mixing. *J. Phys. Oceanogr.*, **30**, 550–563.
- Phillips, O. M., 1966: *The Dynamics of the Upper Ocean*. Cambridge University Press, 336 pp.
- Press, W. H., S. A. Teukolsky, W. T. Vetterling, and B. P. Flannery, 1989: *Numerical Recipes in FORTRAN*. Cambridge University Press, 963 pp.
- Rubenstein, D., 1988: Scattering of inertial waves by rough bathymetry. *J. Phys. Oceanogr.*, **18**, 5–18.
- Sandstrom, H., 1976: On topographic generation and coupling of internal waves. *J. Fluid Dyn.*, **7**, 231–270.
- Sjoberg, B., and A. Stigebrandt, 1992: Computing of the geographical distribution of the energy flux to mixing processes via internal tides and the associated vertical circulation in the ocean. *Deep-Sea Res.*, **39** (2), 269–291.